




Partial confinement in a quantum-link simulatorZheng Tang ¹, Fei Zhu,¹ Yi-Fan Luo,^{2,3} Wei Zheng ^{2,3,4,*} and Li Chen ^{1,†}¹*Institute of Theoretical Physics, State Key Laboratory of Quantum Optics and Quantum Optics Devices, Shanxi University, Taiyuan 030006, China*²*Hefei National Laboratory for Physical Sciences at the Microscale and Department of Modern Physics, University of Science and Technology of China, Hefei 230026, China*³*CAS Center for Excellence in Quantum Information and Quantum Physics, University of Science and Technology of China, Hefei 230026, China*⁴*Hefei National Laboratory, University of Science and Technology of China, Hefei 230088, China*

(Received 9 May 2024; accepted 21 August 2024; published 3 September 2024)

Confinement and deconfinement, captivating attributes of high-energy elementary particles, have recently garnered wide attention in quantum simulations based on cold atoms. However, partial confinement, an intermediate state between the confinement and deconfinement, remains underexplored. The partial confinement encapsulates the phenomenon that the confining behavior of charged particles is contingent upon their relative positions. In this paper we demonstrate that the spin-1 quantum-link model provides an excellent platform for exploring partial confinement. We conduct a comprehensive investigation of the physics emerging from partial confinement in the context of both equilibrium and nonequilibrium dynamics. Potential experimental setups using cold atoms are also discussed. Our work offers a simple and feasible routine for the study of confinement-related physics in the state-of-the-art artificial quantum systems subject to gauge symmetries.

DOI: [10.1103/PhysRevA.110.033302](https://doi.org/10.1103/PhysRevA.110.033302)**I. INTRODUCTION**

Confinement is a fundamental property prominently observed in quantum chromodynamics (QCD), where the interquark potential increases with their distance [1–3]. This prevents the existence of isolated quarks due to energetic instability; instead, they tend to bind together into hadrons, either as mesons (quark-antiquark pairs) or baryons (triplets of quarks). Although the concept originated in QCD, analogous phenomena can also manifest in strongly coupled charges in quantum electrodynamics (QED) [4,5], i.e., the charge confinement. Dimensional analysis indicates that the dimensionality of the coupling constant is determined by the dimensions of the system. Specifically for $3 + 1$ dimensions, the coupling constant is dimensionless, leading to a deconfined Coulomb potential of approximately $1/r$, where r is the distance between two charges. The deconfinement-confinement phase transition can occur by tuning the coupling strength and the temperature [6]. However, for $(1 + 1)$ -dimensional QED, also known as the Schwinger model, the dimensionality of the coupling constant scales linearly with r . Consequently, apart from certain exceptional cases, the confining phase becomes quite prevalent. Furthermore, confinement and deconfinement phenomena also appear in emergent gauge theories from strongly correlated electrons and recently developed Rydberg atomic arrays [7–11]. For instance, transition between a valence bond solid to spin liquid phase can be understood in a picture

of confinement-deconfinement transition of spinons [12,13]. However, large-scale numerical investigation of the real time dynamics of confinement or deconfinement on classical computers is challenging.

Recently, much effort has been made to overcome this barrier through quantum simulation [14–24], which leverages systems with discrete degrees of freedom. This includes analog simulations using optical lattices [25–46] or trapped ions [47–50] and digital simulations realized on various quantum computing platforms [51–63]. The quantum-link model (QLM) [64] serves as one of the most commonly used approaches to simulate lattice gauge theories, which are based on the Hamiltonian formalism with space discretized while time remains continuous. In QLMs, matter particles are placed on lattice sites, while gauge spins with a finite local Hilbert space are located on the links connecting neighboring sites. The realization of the QLM is considered a powerful approach for exploring strongly coupled QED, as strong coupling renders perturbative field theory ineffective, and hence quantum simulation can essentially circumvent the issues encountered by classical simulations, such as the sign problem in quantum Monte Carlo methods [65]. In these quantum-link simulators, both confinement and deconfinement have been extensively studied, encompassing theoretical [44,45,66–73] and experimental [30,74] contexts. Particularly for the spin-1/2 QLM, the confinement-deconfinement transition has been experimentally signified in dynamics through tuning the topological angle [30].

In this paper we delve into an intermediate phenomenon between confinement and deconfinement in $(1 + 1)$ -dimensional QED, called partial confinement, within the

*Contact author: zw8796@ustc.edu.cn†Contact author: lchen@sxu.edu.cn

context of quantum simulation. It refers to the situation where the confining or deconfining status between charges depends on their relative positions. Our study draws inspiration from the seminal work of Coleman [5], which studied half-asymptotic particles in the continuum Schwinger model. Here we demonstrate that the one-dimensional spin-1 QLM can serve as an excellent platform for observing partial confinement: It retains the essential physics while being simple enough to be realized within the scope of current experimental capabilities. Taking the spin-1 QLM as a background, we introduce the basic concept of partial confinement and discuss the associated emergent physics in both equilibrium and nonequilibrium dynamics.

It is worth clarifying that the terminology of partial (de)confinement has already been introduced in QCD [75–77]. Therein, partial confinement refers to a phase where color degrees of freedom split into confined and deconfined sectors, with a subgroup of the $SU(N)$ gauge group becoming deconfined while the remainder stays confined. This is typically characterized by a nonuniform distribution of Polyakov loop phases and the N dependence of thermodynamic quantities. As such, this notion of partial confinement carries a different physical meaning compared to ours defined above.

The rest of this paper is structured as follows. Section II provides a review of the spin-1 quantum-link model, detailing its essential physical features. In Sec. III we delve into the equilibrium properties of partial confinement within the spin-1 QLM. Section IV discusses how partial confinement manifests in nonequilibrium dynamics. In Sec. V we explore the feasibility of experimental realizations using cold atoms trapped in optical superlattices. A brief summary is provided in Sec. VI.

II. SPIN-1 QUANTUM-LINK MODEL

The spin-1 quantum-link chain is characterized by the Hamiltonian [44,64,78]

$$H = -J \sum_{j=1}^{N-1} \left(\frac{1}{\sqrt{2}} \psi_j S_j^+ \psi_{j+1} + \text{H.c.} \right) + m \sum_{j=1}^N \psi_j^\dagger \psi_j + g \sum_{j=1}^{N-1} \left((-1)^{j+1} S_j^z + \frac{\theta}{2\pi} \right)^2, \quad (1)$$

where ψ_j denotes the local matter fields of fermions and $S_j^{z,\pm}$ are the spin-1 Pauli operators representing the gauge spins existing on the link between two neighboring sites j and $j+1$. The number of sites N must be even, allowing for the division of fermions into electrons and positrons, yielding the particle-antiparticle picture: For $j \in \text{odd}$, the unoccupied and occupied statuses of electrons are denoted by white circles and blue circles, respectively, in Fig. 1, whereas for $j \in \text{even}$, the corresponding occupation status of positrons are illustrated by white circles and red circles.

The last two terms in H represent the fermion mass with $m \geq 0$ and the electric-field energy $g \sum_j E_j^2$ with $g \geq 0$ and

$$E_j = (-1)^{j+1} S_j^z + \frac{\theta}{2\pi}, \quad (2)$$

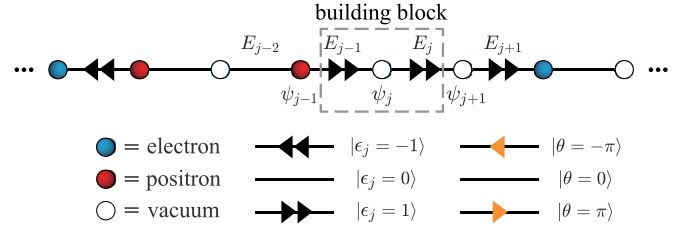


FIG. 1. Shown on top is the schematic representation of a spin-1 quantum-link model in the particle-antiparticle picture. Circles denote matter fields residing on lattice sites; links between neighboring sites represent electric fields E_j realized by gauge spins S_j^z . Two adjacent gauge spins with a matter field in between constitute a building block. Shown on the bottom is the notation convention for matter-field occupations and electric spin states.

respectively. A local E_j consists of two parts. The S_j^z represents the quantized electric field capable of adopting three states $|s_j = -1\rangle$, $|0\rangle$, and $|1\rangle$. The factor $(-1)^j$ indicates that the electric field E_j depends on the gauge spins in an alternating manner: E_j aligns with S_j^z for $j \in \text{odd}$, while they differ by a minus sign for $j \in \text{even}$. The c -number θ is called the topological angle [5,79–81], which reflects the influence of an external static electric field. Thereby, the eigenvalues of E_j can also take three real values, i.e., $\epsilon_j = (-1)^{j+1} s_j^z + \theta/2\pi$. Restricting E_j within a finite status is a key advantage of the QLM, as it facilitates experimental simulation of electric fields using a finite number of discrete degrees of freedom (such as cold atoms with internal spins). In Fig. 1 the black arrows on links represent the electric-field state ϵ_j in the case of $\theta = 0$, where each left- (right-)pointing arrow denotes $\epsilon = -1/2$ ($1/2$). Orange arrows depict the background field of $\pm 1/2$, corresponding to the cases of $\theta = \pm\pi$, respectively. A pair of opposing arrows on the same link can mutually cancel each other out.

The first term in Eq. (1) characterizes the matter-gauge interaction. This term provides the Schwinger mechanism, i.e., a pair of an electron and a positron merge together accompanied by the emission of gauge photons, as well as its reverse process. Photon creation and annihilation are reflected in the change of spin states via S_j^{\pm} .

The spin-1 QLM exhibits a $U(1)$ local gauge symmetry generated by the local Gauss operator

$$G_j = E_j - E_{j-1} - (-1)^j \psi_j^\dagger \psi_j = (-1)^{j+1} (S_j^z + S_{j-1}^z + \psi_j^\dagger \psi_j), \quad (3)$$

satisfying $[G_j, H] = [G_j, G_{k \neq j}] = 0$. This ensures the invariance of the Hamiltonian under arbitrary $U(1)$ gauge transformations $U_j = \exp(i\phi_j G_j)$. As per Eq. (3), G_j is defined within a building block consisting of two gauge fields $\{E_{j-1}, E_j\}$ and a matter field ψ_j in the middle (see the box with dashed lines in Fig. 1). The quantum number of G_j , denoted by q_j , is called the static gauge charge, which is apparently a good quantum number. The q_j characterizes the difference between the net electric flux $E_j - E_{j-1}$ and the matter charge $\psi_j^\dagger \psi_j$. The additional factor $(-1)^j$ arises from the opposite matter charges carried by electrons and positrons. The $U(1)$ gauge symmetry divides the total Hilbert space into

several gauge sectors, each labeled by a unique set of gauge charges $\mathbf{q} = \{q_1, q_2, \dots, q_{N-1}\}$. Notably, the sector with $\mathbf{q} = \mathbf{0}$ is called the physical sector, as now Eq. (3) aligns with the traditional Gauss law in the classical electrodynamics.

In some literature [44,48,82,83], the QLM [Eq. (1)] is presented in an alternative form within the particle picture, described by the Hamiltonian with staggered mass [84,85]

$$\begin{aligned} \tilde{H} = & -J \sum_{j=1}^{N-1} \left(\frac{1}{\sqrt{2}} \psi_j^\dagger S_j^+ \psi_{j+1} + \text{H.c.} \right) \\ & + m \sum_{j=1}^N (-1)^j \psi_j^\dagger \psi_j + g \sum_j \left(S_j^z + \frac{\theta}{2\pi} \right)^2, \end{aligned} \quad (4)$$

which relates to the particle-antiparticle Hamiltonian H [Eq. (1)] through a particle-hole transformation on odd sites, i.e., $\psi_{j \in \text{odd}} \mapsto \psi_{j \in \text{odd}}^\dagger$, as well as a transformation on even gauge spin $S_{j \in \text{even}}^+ \mapsto -S_{j \in \text{even}}^-$ and $S_{j \in \text{even}}^z \mapsto -S_{j \in \text{even}}^z$. In this framework, $\psi_j^\dagger \psi_j$ at odd sites represents the occupation below the Dirac sea, thereby exhibiting a negative energy (mass) $-m$. The creation of a hole ψ_j in the particle picture is equivalent to the creation of an electron ψ_j^\dagger in the particle-antiparticle picture. Note that both Hamiltonians H and \tilde{H} are mathematically equivalent for calculation purposes. Therefore, we proceed with our following analysis using the particle-antiparticle picture.

III. PARTIAL CONFINEMENT IN EQUILIBRIUM

The confining effects can be clearly demonstrated by the properties of equilibrium states in the physical sector $\mathbf{q} = \mathbf{0}$. We first focus on the simplest case of $J = 0$, where the matter and gauge fields are decoupled, thereby $\psi_j^\dagger \psi_j$ and S_j^z being conserved. We insert a pair of a test electron and a positron into the vacuum, separated by a distance d , as schematically shown in Fig. 2(a). The d can be positive or negative, with $d > 0$ indicating the electron is to the left of the positron and vice versa. The case of $d = 0$ is excluded by the Pauli exclusion principle. According to Gauss's law [Eq. (3)], the system is in the string state

$$|\psi_{\text{str}}\rangle = \begin{cases} |\dots 0_0 1_{-1} 0_1 0 \dots 0_1 0_{-1} 1_0 0 \dots\rangle & \text{for } d > 0 \\ |\dots 1_{-1} 0_1 0_{-1} 0 \dots 0_{-1} 1_0 0_0 0 \dots\rangle & \text{for } d < 0, \end{cases} \quad (5)$$

where an electric string exists between the matter charges [see Fig. 2(a)]. The notation convention in a building block is $|s_{j-1}, n_j, s_j\rangle$, with s_j and n_j being the quantum numbers of S_j^z and $\psi_j^\dagger \psi_j$, respectively. For a sufficiently large m , the string state is the ground state, as $m > 0$ does not favor matter-particle excitations.

The confining property is determined by the variance of the state energy $\mathcal{E} = \langle \psi | H | \psi \rangle$ on d , where the topological angle θ plays a crucial role. To be more specific, the string state has energy

$$\mathcal{E}_{\text{str}} = 2m + g|d| \left(-\text{sgn}(d) + \frac{\theta}{2\pi} \right)^2 + g(N - |d| - 1) \left(\frac{\theta}{2\pi} \right)^2, \quad (6)$$

where $\text{sgn}(x)$ is the sign function being defined as $\text{sgn}(x > 0) = 1$ and $\text{sgn}(x < 0) = -1$. When $\theta = 0$, $\mathcal{E}_{\text{str}} = 2m + g|d|$,

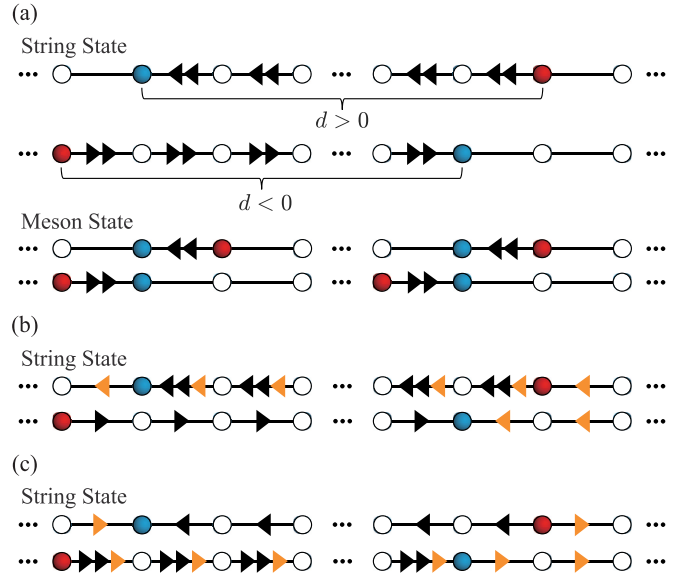


FIG. 2. Configuration of states at $J = 0$. (a) For the case $\theta = 0$, the first and second rows depict the string states with $d > 0$ and $d < 0$, respectively. The third and fourth rows illustrate the corresponding configurations of the meson states. Also shown are the cases (b) $\theta = -\pi$ and (c) $\theta = \pi$, where only the configurations of the string states are shown.

which is linearly proportional to $|d|$, irrelevant to the sign of d , which is the typical nature of confinement. The dependence of \mathcal{E}_{str} on d is numerically confirmed by the line with circles in Fig. 3(a). Pictorially, as depicted in Fig. 2(a), confinement manifests as an increase in the length of the string with local $|\epsilon_j| = 1$, leading to an increment in the total electric energy. The string tension is defined as $\rho = \partial \mathcal{E} / \partial |d|$, which evaluates to $\rho_{\text{str}} = g$ for the string state. The energy instability of the string state manifests in a possible decay into the meson state with lower energy. The meson configuration is

$$|\psi_{\text{meson}}\rangle = \begin{cases} |\dots 0_0 1_{-1} 1_0 0 \dots 0_0 1_{-1} 1_0 0 \dots\rangle & \text{for } d > 0 \\ |\dots 1_{-1} 1_0 0_0 0 \dots 1_{-1} 1_0 0_0 0 \dots\rangle & \text{for } d < 0, \end{cases} \quad (7)$$

as illustrated in Fig. 2(a), which results from the binding of test charges to their nearest antiparticles, with the interparticle electric string being screened. Hence, the decay process is also called the string breaking. The meson state has an energy

$$\mathcal{E}_{\text{meson}} = 4m + 2g \left(-\text{sgn}(d) + \frac{\theta}{2\pi} \right)^2 + g(N - 3) \left(\frac{\theta}{2\pi} \right)^2, \quad (8)$$

which is notably independent of the distance $|d|$. For $\theta = 0$, the energy simplifies to $\mathcal{E}_{\text{meson}} = 4m + 2g$, as indicated by the line with triangles in Fig. 3(a). This implies a transition point

$$d_c = 2 + \frac{2m}{g[1 - \text{sgn}(d)\frac{\theta}{\pi}]}. \quad (9)$$

For $|d| < |d_c|$, the string state $|\psi_{\text{str}}\rangle$ has lower energy, as it involves fewer matter particles compared to the meson state; however, for $|d| > |d_c|$, the meson state becomes more energetically favored. For $\theta = 0$, the transition point is where

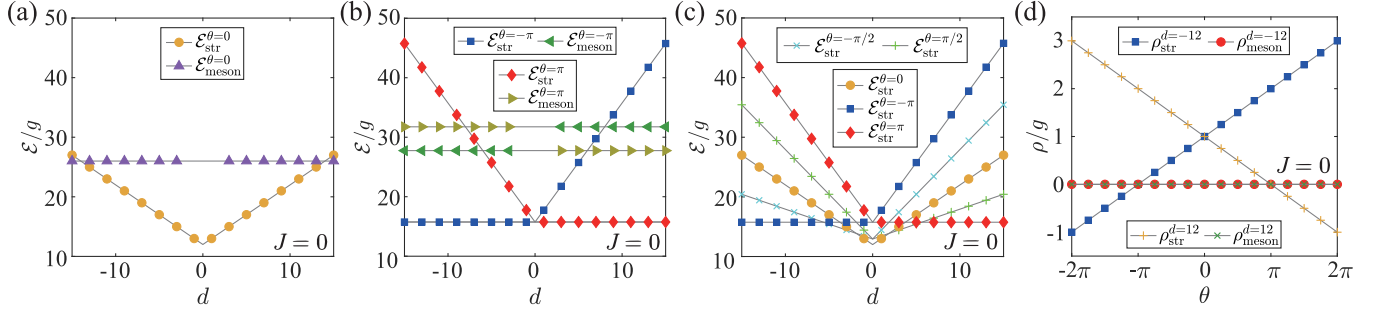


FIG. 3. Equilibrium states' energy \mathcal{E} and string tension ρ in the case of $J = 0$, with $N = 16$, $g = 1$, and $m = 6g$ being fixed. (a) Dependence of the string-state energy \mathcal{E}_{str} and the meson state energy $\mathcal{E}_{\text{meson}}$ on d for $\theta = 0$. (b) Behavior of \mathcal{E}_{str} and $\mathcal{E}_{\text{meson}}$ for $\theta = \pm\pi$. (c) String-state energy \mathcal{E}_{str} for different values of θ . (d) String tension ρ as a function of the topological angle θ for fixed $d = \pm 12$.

the two curves converge with $|d_c| = 2 + 2m/g$, as shown in Fig. 3(a).

Partial confinement occurs at $\theta = -\pi$, where the string-state energy simplifies to

$$\mathcal{E}_{\text{str}}^{\theta=-\pi} = \begin{cases} 2m + g[2d + (N-1)/4] & \text{for } d > 0 \\ 2m + g[(N-1)/4] & \text{for } d < 0. \end{cases} \quad (10)$$

Accordingly, the string tension is $\rho_{\text{str}} = 2g$ for $d > 0$ and $\rho_{\text{str}} = 0$ otherwise. It is clearly indicated that the confining effect only occurs for $d > 0$. For $d < 0$, \mathcal{E}_{str} is independent of d , suggesting a deconfinement with $d_c = \infty$. This phenomenon, that the confining property depends on the relative positions of the opposite charges, is termed partial confinement. Visually, as illustrated in Fig. 2(b), the string states for $d > 0$ and $d < 0$ are subjected to different electric potentials. For the former, the energy density within the string is $g(3/2)^2$, while that of the vacuum is $g(1/2)^2$, resulting in a nonvanishing string tension $\rho_{\text{str}} = 2g$, which is twice the value corresponding to the $\theta = 0$ case. For the latter, the electric fields inside and outside the string have opposite signs but with the same energy density $g(1/2)^2$, thus making \mathcal{E} be $|d|$ invariant. In Fig. 3(b), the line with squares depicts the variation of the string-state energy $\mathcal{E}_{\text{str}}^{\theta=-\pi}$ as a function of d , while the line with left-pointing triangles represents the meson state energy $\mathcal{E}_{\text{meson}}^{\theta=-\pi}$. It is evident that the string breaking can only occur in the confined regime $d > 0$, with $d_c = 2 + m/g$. The value of d_c is smaller compared to the $\theta = 0$ case, as shown in Fig. 2(b), due to the larger string tension.

Partial confinement also occurs at $\theta = \pi$, but the dependence of quantities (such as \mathcal{E} and ρ) on the sign of d is opposite to the case of $\theta = -\pi$, as illustrated in Figs. 2(c) and 3(b) (see lines with diamonds and squares). The underlying mechanism can be understood in the following way. For the Hamiltonian (1), $\theta \rightarrow -\theta$ is equivalent to $S_j^+ \rightarrow S_{j+1}^+$, $S_j^z \rightarrow S_{j+1}^z$, and $\psi_j \rightarrow \psi_{j+1}$, with the latter corresponding to the charge conjugation \mathcal{C} . As a result, the physics under $\theta = -\pi$ with a given d is reproduced by $\theta = \pi$ with $-d$. This suggests that reversing θ alone can switch between confinement and deconfinement scenarios without the need to adjust the spatial ordering of charges. It would facilitate experimental observation of partial confinement since tuning the topological angle (namely, tuning the external field) is generally more accessible than manipulating the particle positions in practice.

For other cases with $\theta \in (-\pi, \pi)$ and $\theta \neq |\pi|$, the string state is generally confined according to Eq. (6), with \mathcal{E}_{str} for various θ being shown in Fig. 3(c). The \mathcal{E}_{str} is asymmetric about $d = 0$, with the corresponding string tension being given by $\rho_{\text{str}} = g[1 - (\theta/\pi)\text{sgn}(d)]$. The asymmetry of $\mathcal{E}(d)$ and $\rho_{\text{str}}(d)$ for $\theta \neq 0$ originates from the breaking of both \mathcal{C} and \mathcal{P} symmetry due to the topological angle θ , where \mathcal{P} is the parity operator acting as $S_j^+ \rightarrow S_{-j-1}^+$, $S_j^z \rightarrow S_{-j-1}^z$, and $\psi_j \rightarrow (-1)^j \psi_{-j}$ on the Hamiltonian (1). In Fig. 3(d) we set $d = \pm 12$ and display the dependence of ρ on θ . One can clearly observe that the partial confinement begins to occur at $\theta = \pm\pi$, where $\rho_{\text{str}} = 0$. For a larger θ , i.e., $|\theta| > \pi$, the string state becomes deconfined with a negative string tension. This is also intuitive, as a strong background electric field would polarize the charging pair and yield a large dipole moment.

The above results for $J = 0$ will not be qualitatively altered when we turn on the matter-gauge interaction J . When J is finite, the system lacks integrability, causing us to resort to numerical calculations. By setting $J = g = 1$ and $m = 6g$, we numerically calculate the energy spectrum of the system. Although quantum fluctuations render s_j^z and n_j no longer good quantum numbers, we can still identify low-energy stringlike and mesonlike states, with the averaged local observables, such as $\langle S_j^z \rangle$ and $\langle \psi_j^\dagger \psi_j \rangle$, resembling the configurations of string and meson states shown in Fig. 3(b). Intuitively, the string remains but is thickened by quantum fluctuations. In Fig. 4(a) we present the energy variance of these two eigenstates \mathcal{E} on d for various θ . Additionally, Fig. 4(b) shows the corresponding string tension ρ as a function of θ for a fixed $d = \pm 12$. A comparison between Figs. 3(b) and 4(a), as well as Figs. 3(d) and 4(b), clearly demonstrates that the main physical results, such as partial confinement and string breaking, are qualitatively preserved for a nonvanishing J .

It may also be necessary to elucidate the differences between the spin-1 QLM discussed here and the spin-1/2 QLM which has been extensively studied both theoretically and experimentally [10,27–30,44,66,67,86,87]. The Hamiltonian of the spin-1/2 QLM has the same form as Eq. (1), but with the spin operators S_j being spin-1/2 Pauli operators (up to a constant factor). In this case, even without an external electric field, the string state is no longer well defined, as there always exist electric strings between the charges (inner string) and outside the charges (outer string). Commonly, the spin-1/2

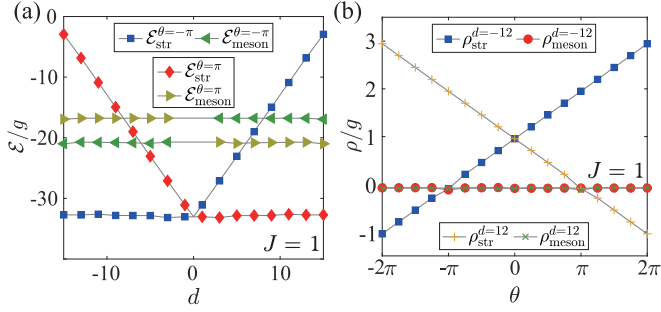


FIG. 4. Equilibrium states' energy \mathcal{E} and string tension ρ in the case of $J = 1$, with all other parameters the same as in Fig. 3. (a) Stringlike eigenstate energy \mathcal{E}_{str} and mesonlike eigenstate energy $\mathcal{E}_{\text{meson}}$ for $\theta = \pm\pi$. (b) String tension as a function of the topological angle θ for fixed $d = \pm 12$.

QLM with the outer string pointing to the right (left) is considered to have an inherent topological angle $\theta = \pi$ ($\theta = -\pi$) [10,30,66,67]. In contrast to the spin-1 case, the charge conjugation \mathcal{C} now would simultaneously change the order of the charges and the sign of θ , rendering the total energy \mathcal{E} irrelevant to the sign of d . In this sense, the spin-1 QLM may serve as a better platform for the study of partial confinement, as it allows for independently changing the charge ordering and θ .

IV. PARTIAL CONFINEMENT IN DYNAMICS

A. String-state dynamics

After discussing equilibrium physics in depth, we now turn to nonequilibrium dynamics. Our objective is to explore whether the physics of partial confinement can be signified by the quantum dynamics out of equilibrium. To this end, we first consider the initial state $|\psi_0\rangle$ to be a string state with the electron and positron residing on the two edges of the chain with $d > 0$, i.e.,

$$|\psi_0\rangle = |\psi_{\text{str}}\rangle = |1_{-1}0_10\cdots 0_10_{-1}\rangle. \quad (11)$$

Notably, this state is an eigenstate of the Hamiltonian H when $J = 0$. We then allow the system to evolve under the government of H with $J = g = 1$. In our numerical simulations, $N = 16$ and $m = 2g = 2$ are fixed. We primarily focus on the three cases of $\theta = \{-\pi, 0, \pi\}$. According to the previous discussion, for such a string configuration $|\psi_0\rangle$ with the electron situated to the left of the positron, both $\theta = 0$ and $\theta = -\pi$ are confining, while $\theta = \pi$ is deconfining. Since flipping the sign of θ is equivalent to changing the sign of charge ordering d , as discussed in Sec. III, comparing the dynamics at $\pm\theta$ for a fixed string state can directly signify the partial confinement.

We begin by examining the expectation values of fermion occupations $\langle n_j \rangle = \langle \psi_j^\dagger \psi_j \rangle$ within the time frame $t \leq 30g^{-1}$, as shown in Fig. 5 for the cases of $\theta = -\pi$ [Fig. 5(a)], $\theta = 0$ [Fig. 5(b)], and $\theta = \pi$ [Fig. 5(c)]. In the figures, the occupations of positrons and electrons are labeled by red and blue bars, respectively. A prominent feature is that, for the first two confining cases, i.e., $\theta = -\pi$ and 0 , the edge charges are locked at the boundaries with almost no movement. In the bulk of the chain, $\langle n_j \rangle$ overall exhibits a periodic oscillation,

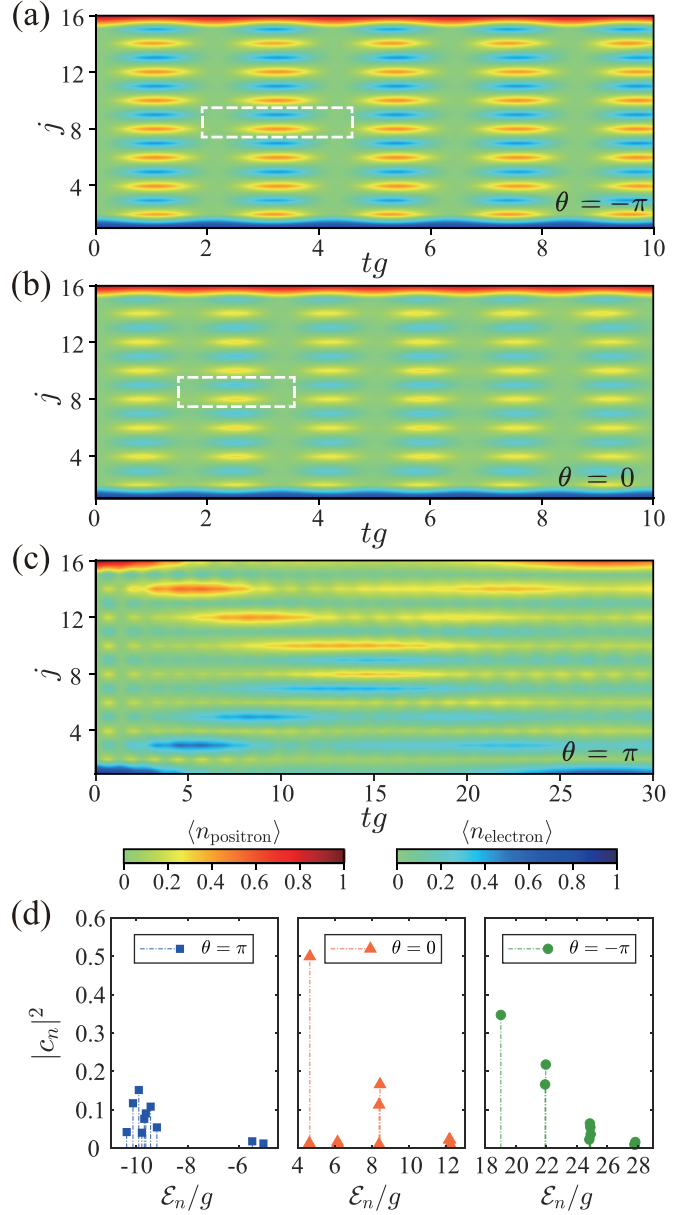


FIG. 5. Density dynamics of the string state. The dynamics of fermion occupations $\langle n_j \rangle$ are shown for (a) $\theta = -\pi$, (b) $\theta = 0$, and (c) $\theta = \pi$, where the occupation status of the positrons and electrons are labeled by the red and blue bars, respectively, the white boxes indicate the Schwinger mechanism. (d) Top ten projection probabilities $|c_n|^2$ of the initial state $|\psi_0\rangle$ on the eigenstates $|n\rangle$ of H for different values of θ . In the calculation, we take $N = 16$, $m = 2g$, and $J = g = 1$.

which is indicative of the Schwinger mechanism, as labeled by the white boxes: Electron-positron pairs are spontaneously created from the vacuum and then rapidly annihilated with each other. The confinement effect is also evidenced by the small lifetime of the emerged particles (antiparticles) and the fact that they cannot propagate to a wider range on the chain.

On the other hand, the case with $\theta = \pi$ [Fig. 5(c)] exhibits a strikingly different behavior. The two edge charges move towards each other until they meet at the center of the chain at about $t \approx 12g^{-1}$; after that, they reverse their directions

and retreat to the boundaries. Unlike the traditional scattering process for free fermions where transmitted waves continue to propagate forward after the scattering event, here we do not observe a clear signal of transmitted wave propagation. Additionally, it can be also notable from the figure that the particle occupation $\langle n_j \rangle$ at the boundaries is significantly decreased compared to the initial state after one round-trip. Unlike the Schwinger oscillations in the former two cases, the back-and-forth motion of particles can now only sustain for a few cycles and lacks robust periodicity.

To quantitatively explain the periodicity of $\langle n_j \rangle$ in Fig. 5, we calculate the projection probabilities of the initial state, defined as $|c_n|^2 = |\langle n | \psi_0 \rangle|^2$, where $|n\rangle$ is the eigenstate of H with energy \mathcal{E}_n . In Fig. 5(d), the ten largest values of $|c_n|^2$ are plotted against \mathcal{E}_n , with different θ values indicated using different markers. For comparison, we have aligned the ground state energy \mathcal{E}_0 of different θ values by shifting the spectra. From the data, it is evident that for $\theta = 0$ and $\theta = -\pi$, the initial state $|\psi_0\rangle$ is primarily composed of three high-energy eigenstates. These eigenstates exhibit a definite energy gap $\Delta\mathcal{E}$, which determines the oscillating period of $\langle n_j \rangle$ in the way of $T = 2\pi/\Delta\mathcal{E}$. Specifically, for $\theta = 0$, $\Delta\mathcal{E} \approx 3.78g$ and $T \approx 1.66g^{-1}$, whereas for $\theta = -\pi$, $\Delta\mathcal{E} \approx 2.95g$ and $T \approx 2.13g^{-1}$. On the other hand, for the case of $\theta = \pi$, $|\psi_0\rangle$ consists of a broader spectrum of low-energy eigenstates. These states lack a consistent energy gap, which dictates the aperiodic behavior of $\langle n_j \rangle$.

The confining and deconfining characteristics can also be distinguished from the dynamics of the bipartite entanglement entropy

$$S = -\text{Tr} \rho_R \ln \rho_R, \quad (12)$$

where ρ_R is the reduced density matrix obtained by tracing out the degrees of freedom in one half of the chain. The evolution of S is displayed in Fig. 6(a), where the dotted, dashed, and solid lines correspond to $\theta = \{-\pi, 0, \pi\}$, respectively. The data reveal that, for the confining cases with $\theta = \{-\pi, 0\}$, S exhibits periodic oscillations and grows slowly in the time domain $t > 1$; until $t_c \sim 100g^{-1}$, S tends to approach saturation. In contrast, for the deconfining case with $\theta = \pi$, S undergoes a rapid increase in the interval $t \in [1, 10]$, following an approximate power-law scaling. It reaches equilibration at $t_c \sim 10g^{-1}$, which is an order of magnitude smaller compared to the two former cases. The time t_c coincides with the moment when the edge charges propagate to the center of the chain [see Fig. 5(c)].

We also calculate the dynamics of the connected density correlation, defined by

$$\langle n_1 n_N \rangle_{\text{con}} = |\langle \psi_1^\dagger \psi_1 \psi_N^\dagger \psi_N \rangle - \langle \psi_1^\dagger \psi_1 \rangle \langle \psi_N^\dagger \psi_N \rangle|, \quad (13)$$

with the results being presented in Fig. 6(b). Here $\langle n_1 n_N \rangle_{\text{con}}$ quantifies the density-density correlation between the matter charges on the edges of the chain. Again, various line styles correspond to different cases of θ . It is anticipated that $\langle n_1 n_N \rangle_{\text{con}} = 0$ at $t = 0$, since the initial state is a product state. The weak correlation can persist for a considerable duration until t_c , beyond which significant correlations between the edge particles begin to develop. For the confining cases with $\theta = \{0, -\pi\}$, t_c is larger than $10^2 g^{-1}$. However, for the deconfining case $\theta = -\pi$, $t_c \sim 10g^{-1}$, being one order of

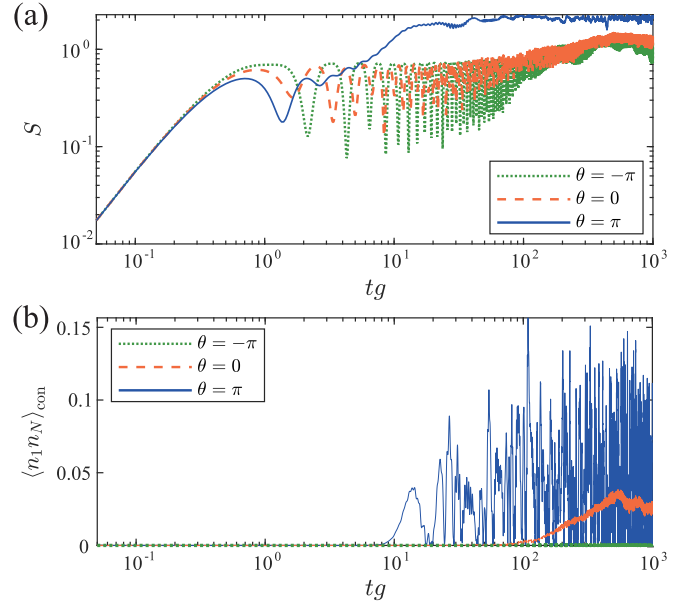


FIG. 6. Dynamics of the entanglement and the correlator for the string state. (a) Dynamics of the bipartite entanglement entropy S for various cases of θ . For the confining cases, S exhibits periodic oscillations and grows slowly due to Schwinger oscillation. In contrast, for the deconfining case, S presents a rapid increase. (b) Dynamics of the density-density correlator $\langle n_1 n_N \rangle_{\text{con}}$ between the two boundary fermions. For the confining cases, only weak correlation persisted. In contrast, for the deconfining case, correlation can grow rapidly. The parameters are $N = 16$, $m = 2J$, and $J = g = 1$.

magnitude smaller than in the previous cases. Therefore, the evolution of edge correlations provides a valuable metric for discerning different confinement statuses.

B. Meson-state dynamics

Up to now, our discussion has focused on the quench dynamics of the string state. Here we additionally consider a scenario where the initial state exhibits a single meson excitation with $d > 0$ at the center of the ground state, i.e.,

$$|\psi_0\rangle = |\psi_{\text{meson}}\rangle = \psi_{N/2}^\dagger S_{N/2}^- \psi_{N/2+1}^\dagger |\psi_g\rangle, \quad (14)$$

where the $|\psi_g\rangle$ is the ground state of the Hamiltonian H [Eq. (1)] for $m = 4g$ and $J = g = 1$. The additional gauge-spin flip $S_{N/2}^-$ ensures that $|\psi_0\rangle$ remains within the physical gauge sector. Since $d > 0$, the particle-antiparticle pair is confined for $\theta = \{-\pi, 0\}$ and deconfined for $\theta = \pi$. We simulate the dynamics of $|\psi_0\rangle$, with the results of the fermion occupations $\langle n_j \rangle$ presented in Fig. 7 for the cases $\theta = -\pi$ [Fig. 7(a)], $\theta = 0$ [Fig. 7(b)], and $\theta = \pi$ [Fig. 7(c)].

One can observe that $\langle n_j \rangle$ exhibits distinct behaviors for different values of θ . Specifically, in the case of strong confinement at $\theta = -\pi$, the meson state remains stuck in the center of the chain without movement. For the relatively weak confining case with $\theta = 0$, the meson simultaneously moves towards both ends of the chain, ensuring conservation of momentum. Thus, for these two confining cases, the positron and electron are bound together. In contrast, for the deconfining

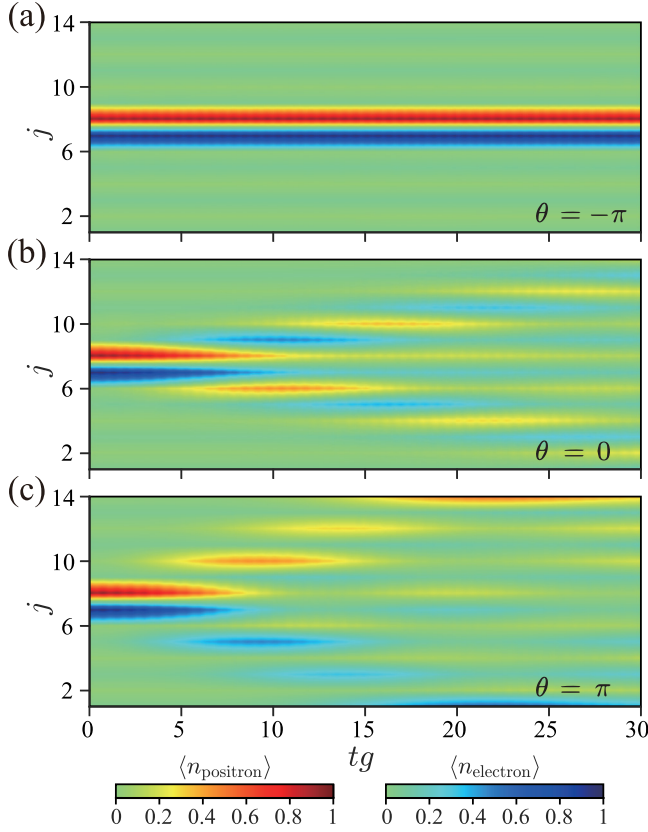


FIG. 7. Density dynamics of the meson state in the cases (a) $\theta = -\pi$, (b) $\theta = 0$, and (c) $\theta = \pi$, where the occupation statuses of the positrons and electrons are labeled by the red and blue bars, respectively. In the calculation, we set $N = 14$, $m = 4g$, and $J = g = 1$.

case of $\theta = \pi$, the meson dissociates into an isolated positron and electron, which then independently move away from each other.

The distinction between the confining and deconfining cases can also manifest in the correlation function [66]

$$\mathcal{G}(r, t) = \sum_{j=1}^N \langle \psi_0(t) | (n_j - \bar{n}_j)(n_{j+r} - \bar{n}_{j+r}) | \psi_0(t) \rangle, \quad (15)$$

where $n_j = \psi_j^\dagger \psi_j$ and $\bar{n}_j = \langle \psi_g | n_j | \psi_g \rangle$. Here $\mathcal{G}(r, t)$ quantifies the spatial correlation of density fluctuations between any two arbitrary lattice sites separated by a distance r . The numerical results of $\mathcal{G}(r, t)$ for various values of θ are shown in Fig. 8. Specifically, for the confining cases with $\theta = \{0, -\pi\}$, the correlation function $\mathcal{G}(r, t)$ remains localized and does not diffuse as t increases. In contrast, for the deconfining case with $\theta = \pi$, the correlation function between the positron and electron can propagate at a considerable speed and eventually spread throughout the entire space.

V. EXPERIMENTAL CONSIDERATION

We finally discuss the potential experimental realization using ultracold atoms. The spin-1 QLM has been theoretically proposed to be engineered from a generalized Bose-Hubbard model (BHM) [88], which can be implemented with ultracold bosonic gases confined in a superlattice, as illustrated

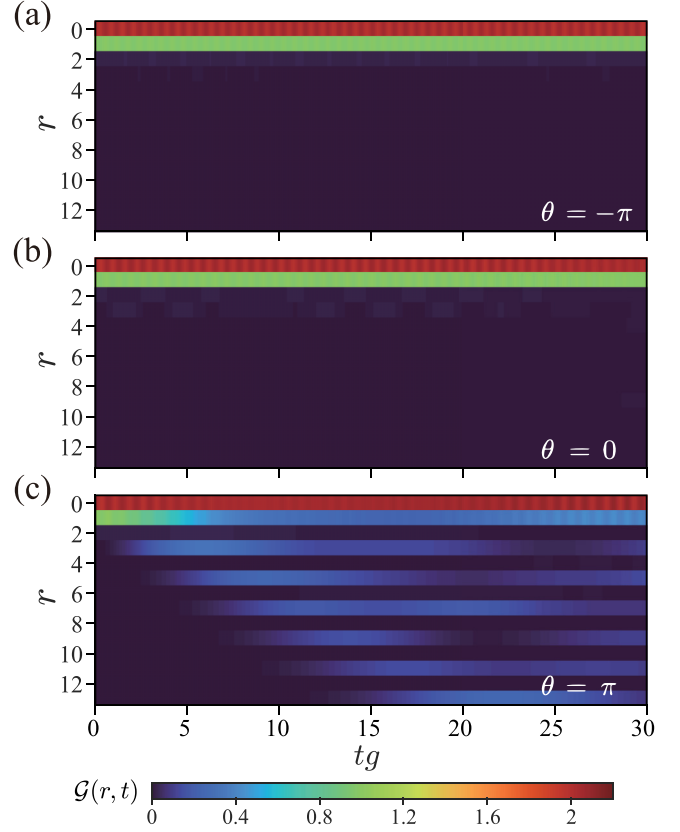


FIG. 8. Dynamics of the correlation function for the meson state in the cases (a) $\theta = -\pi$, (b) $\theta = 0$, and (c) $\theta = \pi$, with all the parameters the same as in Fig. 7.

in Fig. 9(a). Specifically, the atomic gas is governed by the Hamiltonian

$$\begin{aligned} H_{\text{BHM}} = & -\tilde{J} \sum_{l=1}^{L-1} (b_l^\dagger b_{l+1} + \text{H.c.}) + \frac{U}{2} \sum_{l=1}^L n_l(n_l - 1) \\ & + \sum_{l=1}^L \left((-1)^l \frac{\delta}{2} + l\gamma + \frac{\chi_l}{2} \right) n_l + V \sum_{l=1}^{L-1} n_l n_{l+1} \\ & + W \sum_{l=1}^{L/2-1} n_{2l-1} n_{2l+1}, \end{aligned} \quad (16)$$

where $L = 2N$ is the total number of lattice sites, b_l and b_l^\dagger are local bosonic operators satisfying $[b_k, b_l^\dagger] = \delta_{k,l}$, and $n_l = b_l^\dagger b_l$. In addition, \tilde{J} is the hopping between neighboring sites, δ creates energy offsets between matter sites and gauge spins, and γ serves as a tilted potential. The δ and γ help to eliminate gauge-breaking hoppings. Further, χ_l is a four-site periodic term employed to realize the topological angle [67], i.e.,

$$\chi_l = \begin{cases} 0 & \text{if } l \bmod 2 = 0 \\ \chi & \text{if } l \bmod 4 = 1 \\ -\chi & \text{if } l \bmod 4 = 3, \end{cases} \quad (17)$$

where $\chi = g\theta/\pi$. In the second line of Eq. (16), U is the on-site interaction and V and W are the nearest-neighbor and next-nearest-neighbor interactions, respectively.

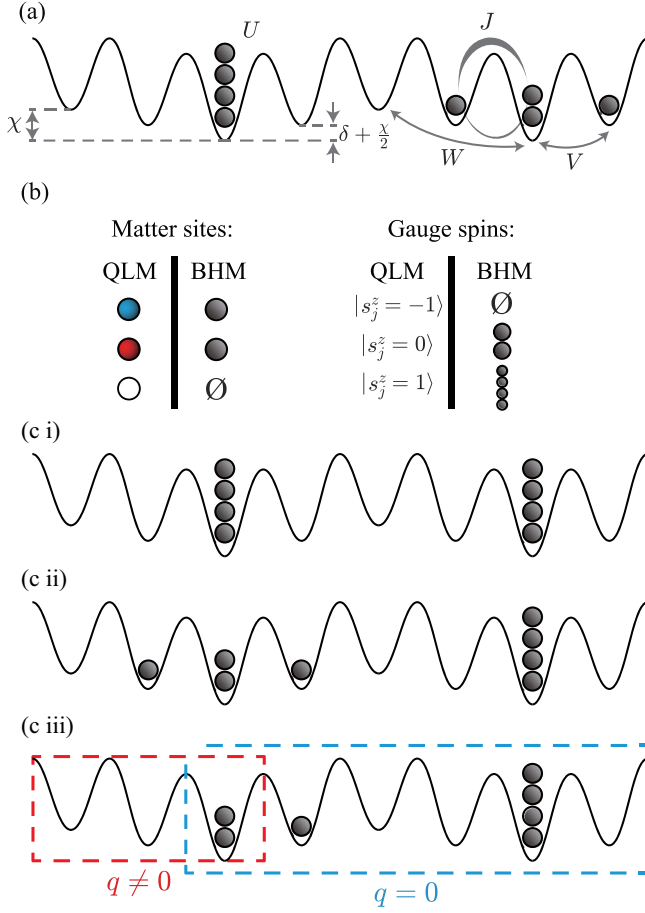


FIG. 9. (a) Schematics of BHM simulator on a one-dimensional superlattice, where the tilted potential γ is not shown. (b) Mapping relations between the particle representation of the BHM occupation and the particle-antiparticle picture of the QLM. (c) Preparation of the string state, with only the left boundary shown. (c i) Extreme vacuum state. (c ii) Local particle-antiparticle pairs are generated using single-site addressing techniques. (c iii) The string state is obtained by removing the outer particles. Blue and red boxes indicate the physical and nonphysical gauge sectors, respectively, with the latter providing a hard-wall boundary for the former.

The generalized Bose-Hubbard model [Eq. (16)] serves as the foundation for realizing the spin-1 QLM [Eq. (1)] of length N . In this setup, the even lattice sites with $l \in \text{even}$ can only be singly occupied or empty, representing matter particles, whereas the occupancies at odd sites are restricted to $n_{l \in \text{odd}} = \{0, 2, 4\}$ to realize the three gauge-spin states. The detailed mapping relations between the two models are presented in Fig. 9(b). To realize the gauge invariance in the $\mathbf{q} = \mathbf{0}$ sector, we focus on the three configurations

$$\begin{aligned} |C_1\rangle &= |0400\rangle_{\text{BHM}} \leftrightarrow |0_1 0_{-1}\rangle_{\text{QLM}}, \\ |C_2\rangle &= |1210\rangle_{\text{BHM}} \leftrightarrow |1_0 1_{-1}\rangle_{\text{QLM}}, \\ |C_3\rangle &= |0202\rangle_{\text{BHM}} \leftrightarrow |0_0 0_0\rangle_{\text{QLM}}, \end{aligned} \quad (18)$$

where $|n_l, n_{l+1}, n_{l+2}, n_{l+3}\rangle_{\text{BHM}}$ denotes the particle number representation of the BHM occupation status of four consecutive sites for $l \in \text{even}$ and $|n_j, s_{j+1}, n_{j+2}, s_{j+3}\rangle_{\text{QLM}}$ represents the corresponding matter and gauge configuration in the

QLM, where $j = l/2$. When $\tilde{J} = 0$, the bare energies of the three configurations $|C_{1,2,3}\rangle$ are

$$\begin{aligned} \mathcal{E}_1 &= 6U - 2\delta \pm 2\chi, & \mathcal{E}_2 &= U + 4V \pm \chi, \\ \mathcal{E}_3 &= 2U + 8W - 2\delta, \end{aligned} \quad (19)$$

where the \pm determined by the bosonic lattice site index l according to Eq. (17). Based on this, all head-to-tail combinations of the three configurations span the entire Hilbert space in the physical sector.

Notably, there exist configurations that do not preserve gauge invariance. To circumvent these states, it is necessary to ensure that the bare energies of gauge-invariant configurations are nearly resonant, while those of the gauge-violating configurations are far detuned from resonance. In the case of $U, V, W, \gamma \gg \tilde{J}$, it requires that

$$V \approx \frac{5U}{4} - \frac{\delta}{2}, \quad W \approx -\frac{U}{2} + \delta + 2V \approx 2U. \quad (20)$$

By applying the Schrieffer-Wolff transformation, we can derive the effective Hamiltonian of the Bose-Hubbard model within the gauge-invariant subspace, which takes the form of Eq. (1). The detailed coefficient relations are given by

$$g = 2U - 4W, \quad (21a)$$

$$m = -\frac{3}{2}U + \delta + 2V - 2W, \quad (21b)$$

$$J = \frac{8\sqrt{12}\tilde{J}^2(2\delta - 3U)}{(2\delta - 3U)^2 - 16\gamma^2}, \quad (21c)$$

where we have omitted the term proportional to \tilde{J}^2 in Eqs. (21a) and (21b) due to the perturbative nature of J . Additionally, χ is considered negligible in the expression of Eq. (21c) as $|\delta \pm \gamma| \gg |\chi|$ is satisfied [67].

The extreme vacuum state $|\psi_{\text{ev}}\rangle$ forms the basis for preparing string states, which is defined by

$$|\psi_{\text{ev}}\rangle = |\cdots 0400 \cdots\rangle_{\text{BHM}} \leftrightarrow |\cdots 0_1 0_{-1} \cdots\rangle_{\text{QLM}}. \quad (22)$$

This state, as shown in Fig. 9(c i), can be prepared systematically following a well-defined protocol [26,67,89]. The protocol begins with the system in a uniform superfluid (SF) state. The lattice potential is then gradually modified to establish the desired staggered structure by ramping the parameters γ and χ . Following this, the ratio U/\tilde{J} is tuned to induce a phase transition from the SF to a Mott insulator state, where deep lattice sites achieve a four-particle occupancy, shallow sites remain vacant, and even sites have an average occupancy satisfying $0 < \langle n_{l \in \text{even}} \rangle < 4$. Thereafter, spin-selective techniques [89] are applied to selectively remove particles from the even sites, resulting in the formation of the extreme vacuum state.

The string state $|\psi_{\text{str}}\rangle$ [Eq. (11)] is distinguished from $|\psi_{\text{ev}}\rangle$ by modifications only at the boundaries. Employing single-site addressing techniques [26,67,90] enables the generation of particle-antiparticle pairs at the boundaries of the vacuum state, as depicted in Fig. 9(c ii). Subsequently, by locally removing the outer particles through a laser-induced resonant excitation, the string state can ultimately be obtained, as shown in Fig. 9(c iii). At the left end of the chain, the left outer gauge sector (enclosed by the red box), with

configuration $|012\cdots\rangle_{\text{BHM}} \leftrightarrow |_{-1}0_0\cdots\rangle_{\text{QLM}}$, does not belong to the physical sector $q = 0$. This ensures that the rest of the chain (marked by the blue frame) operates consistently within the physical sector and experiences a hard-wall boundary. A similar strategy is also employed at the right end of the chain to achieve the complete particle distribution and boundary condition required for the string state.

VI. CONCLUSION

We have presented a comprehensive investigation of partial confinement on the platform of the spin-1 quantum-link model, a promising platform realizable with cold atoms in optical superlattices. The partial confinement is characterized by a dependence of confinement properties on the spatial arrangement of charged particles, manifested by the asymmetry of the equilibrium energy and the string tension of the string state with respect to the charge ordering. In the nonequilibrium dynamics, both string and meson states exhibit strikingly distinct dynamical features depending on their (de)confining status, as reflected in quantities such as

local fermion occupations, bipartite entanglement entropy, and edge charge correlations. We have also elucidated that manipulating the topological angle can be an effective proxy for controlling charge ordering, thereby simplifying experimental procedures by obviating the need for direct charge manipulation. Given that the quantum-link model is amenable to current experimental capabilities, our study offers a strategic avenue for exploring novel physics in gauge theories using state-of-the-art quantum simulators. Furthermore, it may also be interesting to discuss the partial confinement in other forms of lattice gauge theories such as the improved Hamiltonian [91,92].

ACKNOWLEDGMENTS

L.C. acknowledges supports from the NSF of China (Grant No. 12174236) and from the fund for the Shanxi 1331 Project. W.Z. acknowledges support from the NSF of China (Grants No. GG2030007011 and No. GG2030040453) and Innovation Program for Quantum Science and Technology (Grant No. 2021ZD0302004).

-
- [1] K. G. Wilson, Confinement of quarks, *Phys. Rev. D* **10**, 2445 (1974).
- [2] C. G. Allan, R. Dashen, and D. J. Gross, A mechanism for quark confinement, *Phys. Lett.* **66B**, 375 (1977).
- [3] J. Greensite, *An Introduction to the Confinement Problem*, Lecture Notes in Physics Vol. 821 (Springer, Berlin, 2011).
- [4] J. Schwinger, Gauge invariance and mass, *Phys. Rev.* **125**, 397 (1962).
- [5] S. Coleman, More about the massive Schwinger model, *Ann. Phys. (NY)* **101**, 239 (1976).
- [6] B. Svetitsky, Symmetry aspects of finite-temperature confinement transitions, *Phys. Rep.* **132**, 1 (1986).
- [7] Y. Cheng and H. Zhai, Emergent U(1) lattice gauge theory in Rydberg atom arrays, *Nat. Rev. Phys.* (2024), doi:10.1038/s42254-024-00749-6.
- [8] Y. Cheng, C. Li, and H. Zhai, Variational approach to quantum spin liquid in a Rydberg atom simulator, *New J. Phys.* **25**, 033010 (2023).
- [9] L. Pan and H. Zhai, Composite spin approach to the blockade effect in Rydberg atom arrays, *Phys. Rev. Res.* **4**, L032037 (2022).
- [10] F. M. Surace, P. P. Mazza, G. Giudici, A. Lerose, A. Gambassi, and M. Dalmonte, Lattice gauge theories and string dynamics in Rydberg atom quantum simulators, *Phys. Rev. X* **10**, 021041 (2020).
- [11] D. Malz and J. I. Cirac, Few-body analog quantum simulation with Rydberg-dressed atoms in optical lattices, *PRX Quantum* **4**, 020301 (2023).
- [12] S. Sachdev, *Colloquium*: Order and quantum phase transitions in the cuprate superconductors, *Rev. Mod. Phys.* **75**, 913 (2003).
- [13] Z. Alpichshev, F. Mahmood, G. Cao, and N. Gedik, Confinement-deconfinement transition as an indication of spin-liquid-type behavior in Na_2IrO_3 , *Phys. Rev. Lett.* **114**, 017203 (2015).
- [14] U. Wiese, Ultracold quantum gases and lattice systems: Quantum simulation of lattice gauge theories, *Ann. Phys. (Berlin)* **525**, 777 (2013).
- [15] M. C. Bañuls, R. Blatt, J. Catani, A. Celi, J. I. Cirac, M. Dalmonte, L. Fallani, K. Jansen, M. Lewenstein, S. Montangero, C. A. Muschik, B. Reznik, E. Rico, L. Tagliacozzo, K. Van Acoleyen, F. Verstraete, U.-J. Wiese, M. Wingate, J. Zakrzewski, and P. Zoller, Simulating lattice gauge theories within quantum technologies, *Eur. Phys. J. D* **74**, 165 (2020).
- [16] E. Zohar, J. I. Cirac, and B. Reznik, Quantum simulations of lattice gauge theories using ultracold atoms in optical lattices, *Rep. Prog. Phys.* **79**, 014401 (2016).
- [17] L. Chen, F. Zhu, Z. Tang, and C. Gao, Ultracold quantum simulation of high-energy physics: Lattice gauge theory and its realization in cold atoms, *Emerging Sci. Tech.* **2**, 49 (2023).
- [18] C. W. Bauer, Z. Davoudi, A. B. Balantekin, T. Bhattacharya, M. Carena, W. A. de Jong, P. Draper, A. El-Khadra, N. Gemelke, M. Hanada *et al.*, Quantum simulation for high-energy physics, *PRX Quantum* **4**, 027001 (2023).
- [19] E. Zohar, Quantum simulation of lattice gauge theories in more than one space dimension—requirements, challenges and methods, *Philos. Trans. R. Soc. A* **380**, 20210069 (2022).
- [20] J. C. Halimeh and P. Hauke, Reliability of lattice gauge theories, *Phys. Rev. Lett.* **125**, 030503 (2020).
- [21] J. C. Halimeh, V. Kasper, and P. Hauke, Fate of lattice gauge theories under decoherence, *arXiv:2009.07848*.
- [22] J. Bender, P. Emonts, and J. I. Cirac, Variational Monte Carlo algorithm for lattice gauge theories with continuous gauge groups: A study of $(2+1)$ -dimensional compact QED with dynamical fermions at finite density, *Phys. Rev. Res.* **5**, 043128 (2023).
- [23] M. Aidelsburger, L. Barbiero, A. Bermudez, T. Chanda, A. Dauphin, D. González-Cuadra, P. R. Grzybowski, S. Hands, F. Jendrzejewski, J. Jünemann *et al.*, Cold atoms meet lattice gauge theory, *Philos. Trans. R. Soc. A* **380**, 20210064 (2022).
- [24] N. Klco, A. Roggero, and M. J. Savage, Standard model physics and the digital quantum revolution: thoughts about the interface, *Rep. Prog. Phys.* **85**, 064301 (2022).

- [25] F. M. Surace, P. Fromholz, N. D. O'pong, M. Dalmonte, and M. Aidelsburger, *Ab initio* derivation of lattice-gauge-theory dynamics for cold gases in optical lattices, *PRX Quantum* **4**, 020330 (2023).
- [26] B. Yang, H. Sun, R. Ott, H.-Y. Wang, T. V. Zache, J. C. Halimeh, Z.-S. Yuan, P. Hauke, and J.-W. Pan, Observation of gauge invariance in a 71-site Bose–Hubbard quantum simulator, *Nature (London)* **587**, 392 (2020).
- [27] A. Mil, T. V. Zache, A. Hegde, A. Xia, R. P. Bhatt, M. K. Oberthaler, P. Hauke, J. Berges, and F. Jendrzejewski, A scalable realization of local U(1) gauge invariance in cold atomic mixtures, *Science* **367**, 1128 (2020).
- [28] Z.-Y. Zhou, G.-X. Su, J. C. Halimeh, R. Ott, H. Sun, P. Hauke, B. Yang, Z.-S. Yuan, J. Berges, and J.-W. Pan, Thermalization dynamics of a gauge theory on a quantum simulator, *Science* **377**, 311 (2022).
- [29] H.-Y. Wang, W.-Y. Zhang, Z. Yao, Y. Liu, Z.-H. Zhu, Y.-G. Zheng, X.-K. Wang, H. Zhai, Z.-S. Yuan, and J.-W. Pan, Interrelated thermalization and quantum criticality in a lattice gauge simulator, *Phys. Rev. Lett.* **131**, 050401 (2023).
- [30] W.-Y. Zhang, Y. Liu, Y. Cheng, M.-G. He, H.-Y. Wang, T.-Y. Wang, Z.-H. Zhu, G.-X. Su, Z.-Y. Zhou, Y.-G. Zheng, H. Sun, B. Yang, P. Hauke, W. Zheng, J. C. Halimeh, Z.-S. Yuan, and J.-W. Pan, Observation of microscopic confinement dynamics by a tunable topological θ -angle, [arXiv:2306.11794](https://arxiv.org/abs/2306.11794).
- [31] D. González-Cuadra, E. Zohar, and J. I. Cirac, Quantum simulation of the Abelian-Higgs lattice gauge theory with ultracold atoms, *New J. Phys.* **19**, 063038 (2017).
- [32] L. Homeier, A. Bohrdt, S. Linsel, E. Demler, J. C. Halimeh, and F. Grusdt, Realistic scheme for quantum simulation of \mathbb{Z}_2 lattice gauge theories with dynamical matter in $(2 + 1)D$, *Commun. Phys.* **6**, 127 (2023).
- [33] L. Tagliacozzo, A. Celi, P. Orland, M. W. Mitchell, and M. Lewenstein, Simulation of non-Abelian gauge theories with optical lattices, *Nat. Commun.* **4**, 2615 (2013).
- [34] J. C. Halimeh, M. Aidelsburger, F. Grusdt, P. Hauke, and B. Yang, Cold-atom quantum simulators of gauge theories, [arXiv:2310.12201](https://arxiv.org/abs/2310.12201).
- [35] T. V. Zache, F. Hebenstreit, F. Jendrzejewski, M. K. Oberthaler, J. Berges, and P. Hauke, Quantum simulation of lattice gauge theories using Wilson fermions, *Quantum Sci. Technol.* **3**, 034010 (2018).
- [36] K. Stannigel, P. Hauke, D. Marcos, M. Hafezi, S. Diehl, M. Dalmonte, and P. Zoller, Constrained dynamics via the Zeno effect in quantum simulation: Implementing non-Abelian lattice gauge theories with cold atoms, *Phys. Rev. Lett.* **112**, 120406 (2014).
- [37] W. Zheng and P. Zhang, Floquet engineering of a dynamical \mathbb{Z}_2 lattice gauge field with ultracold atoms, [arXiv:2011.01500](https://arxiv.org/abs/2011.01500).
- [38] E. Zohar, J. I. Cirac, and B. Reznik, Cold-atom quantum simulator for SU(2) Yang-Mills lattice gauge theory, *Phys. Rev. Lett.* **110**, 125304 (2013).
- [39] R. Dasgupta and I. Raychowdhury, Cold-atom quantum simulator for string and hadron dynamics in non-Abelian lattice gauge theory, *Phys. Rev. A* **105**, 023322 (2022).
- [40] L. Barbiero, C. Schweizer, M. Aidelsburger, E. Demler, N. Goldman, and F. Grusdt, Coupling ultracold matter to dynamical gauge fields in optical lattices: From flux attachment to \mathbb{Z}_2 lattice gauge theories, *Sci. Adv.* **5**, eaav7444 (2019).
- [41] Y. Kuno, K. Kasamatsu, Y. Takahashi, I. Ichinose, and T. Matsui, Real-time dynamics and proposal for feasible experiments of lattice gauge–Higgs model simulated by cold atoms, *New J. Phys.* **17**, 063005 (2015).
- [42] J. C. Halimeh, R. Ott, I. P. McCulloch, B. Yang, and P. Hauke, Robustness of gauge-invariant dynamics against defects in ultracold-atom gauge theories, *Phys. Rev. Res.* **2**, 033361 (2020).
- [43] N. Goldman, G. Juzeliūnas, P. Öhberg, and I. B. Spielman, Light-induced gauge fields for ultracold atoms, *Rep. Prog. Phys.* **77**, 126401 (2014).
- [44] D. Banerjee, M. Dalmonte, M. Müller, E. Rico, P. Stebler, U.-J. Wiese, and P. Zoller, Atomic quantum simulation of dynamical gauge fields coupled to fermionic matter: From string breaking to evolution after a quench, *Phys. Rev. Lett.* **109**, 175302 (2012).
- [45] E. Zohar and B. Reznik, Confinement and lattice quantum-electrodynamic electric flux tubes simulated with ultracold atoms, *Phys. Rev. Lett.* **107**, 275301 (2011).
- [46] E. Zohar, J. I. Cirac, and B. Reznik, Simulating $(2 + 1)$ -dimensional lattice QED with dynamical matter using ultracold atoms, *Phys. Rev. Lett.* **110**, 055302 (2013).
- [47] Z. Davoudi, M. Hafezi, C. Monroe, G. Pagano, A. Seif, and A. Shaw, Towards analog quantum simulations of lattice gauge theories with trapped ions, *Phys. Rev. Res.* **2**, 023015 (2020).
- [48] P. Hauke, D. Marcos, M. Dalmonte, and P. Zoller, Quantum simulation of a lattice Schwinger model in a chain of trapped ions, *Phys. Rev. X* **3**, 041018 (2013).
- [49] O. Băzăvan, S. Saner, E. Tirrito, G. Araneda, R. Srinivas, and A. Bermudez, Synthetic \mathbb{Z}_2 gauge theories based on parametric excitations of trapped ions, *Commun. Phys.* **7**, 229 (2024).
- [50] R. Blatt and C. F. Roos, Quantum simulations with trapped ions, *Nat. Phys.* **8**, 277 (2012).
- [51] E. Zohar, A. Farace, B. Reznik, and J. I. Cirac, Digital lattice gauge theories, *Phys. Rev. A* **95**, 023604 (2017).
- [52] N. Klco, E. F. Dumitrescu, A. J. McCaskey, T. D. Morris, R. C. Pooser, M. Sanz, E. Solano, P. Lougovski, and M. J. Savage, Quantum-classical computation of Schwinger model dynamics using quantum computers, *Phys. Rev. A* **98**, 032331 (2018).
- [53] N. Klco, M. J. Savage, and J. R. Stryker, SU(2) non-Abelian gauge field theory in one dimension on digital quantum computers, *Phys. Rev. D* **101**, 074512 (2020).
- [54] T. Byrnes and Y. Yamamoto, Simulating lattice gauge theories on a quantum computer, *Phys. Rev. A* **73**, 022328 (2006).
- [55] S. V. Mathis, G. Mazzola, and I. Tavernelli, Toward scalable simulations of lattice gauge theories on quantum computers, *Phys. Rev. D* **102**, 094501 (2020).
- [56] C. Muschik, M. Heyl, E. Martinez, T. Monz, P. Schindler, B. Vogell, M. Dalmonte, P. Hauke, R. Blatt, and P. Zoller, U(1) Wilson lattice gauge theories in digital quantum simulators, *New J. Phys.* **19**, 103020 (2017).
- [57] C. Kokail, C. Maier, R. Van Bijnen, T. Brydges, M. K. Joshi, P. Jurcevic, C. A. Muschik, P. Silvi, R. Blatt, C. F. Roos, and P. Zoller, Self-verifying variational quantum simulation of lattice models, *Nature (London)* **569**, 355 (2019).
- [58] E. A. Martinez, C. A. Muschik, P. Schindler, D. Nigg, A. Erhard, M. Heyl, P. Hauke, M. Dalmonte, T. Monz, P. Zoller, and R. Blatt, Real-time dynamics of lattice gauge theories with a few-qubit quantum computer, *Nature (London)* **534**, 516 (2016).

- [59] Z. Davoudi, N. M. Linke, and G. Pagano, Toward simulating quantum field theories with controlled phonon-ion dynamics: A hybrid analog-digital approach, *Phys. Rev. Res.* **3**, 043072 (2021).
- [60] W. A. de Jong, K. Lee, J. Mulligan, M. Płoskoń, F. Ringer, and X. Yao, Quantum simulation of nonequilibrium dynamics and thermalization in the Schwinger model, *Phys. Rev. D* **106**, 054508 (2022).
- [61] A. Kan and Y. Nam, Lattice quantum chromodynamics and electrodynamics on a universal quantum computer, [arXiv:2107.12769](https://arxiv.org/abs/2107.12769).
- [62] A. F. Shaw, P. Lougovski, J. R. Stryker, and N. Wiebe, Quantum algorithms for simulating the lattice Schwinger model, *Quantum* **4**, 306 (2020).
- [63] A. Sørensen and K. Mølmer, Entanglement and quantum computation with ions in thermal motion, *Phys. Rev. A* **62**, 022311 (2000).
- [64] S. Chandrasekharan and U.-J. Wiese, Quantum link models: A discrete approach to gauge theories, *Nucl. Phys. B* **492**, 455 (1997).
- [65] M. Troyer and U.-J. Wiese, Computational complexity and fundamental limitations to fermionic quantum Monte Carlo simulations, *Phys. Rev. Lett.* **94**, 170201 (2005).
- [66] Y. Cheng, S. Liu, W. Zheng, P. Zhang, and H. Zhai, Tunable confinement-deconfinement transition in an ultracold-atom quantum simulator, *PRX Quantum* **3**, 040317 (2022).
- [67] J. C. Halimeh, I. P. McCulloch, B. Yang, and P. Hauke, Tuning the topological θ -angle in cold-atom quantum simulators of gauge theories, *PRX Quantum* **3**, 040316 (2022).
- [68] E. Zohar, J. I. Cirac, and B. Reznik, Simulating compact quantum electrodynamics with ultracold atoms: Probing confinement and nonperturbative effects, *Phys. Rev. Lett.* **109**, 125302 (2012).
- [69] Y. Cheng and C. Li, Gauge theory description of Rydberg atom arrays with a tunable blockade radius, *Phys. Rev. B* **107**, 094302 (2023).
- [70] B. Buyens, J. Haegeman, H. Verschelde, F. Verstraete, and K. Van Acoleyen, Confinement and string breaking for QED₂ in the Hamiltonian picture, *Phys. Rev. X* **6**, 041040 (2016).
- [71] H.-Y. Qi and W. Zheng, Gauge violation spectroscopy of synthetic gauge theories, *Phys. Rev. Res.* **6**, 013047 (2024).
- [72] M. Kebrič, J. C. Halimeh, U. Schollwöck, and F. Grusdt, Confinement in (1 + 1)-dimensional \mathbb{Z}_2 lattice gauge theories at finite temperature, *Phys. Rev. B* **109**, 245110 (2024).
- [73] M. Kebrič, L. Barbiero, C. Reinmoser, U. Schollwöck, and F. Grusdt, Confinement and Mott transitions of dynamical charges in one-dimensional lattice gauge theories, *Phys. Rev. Lett.* **127**, 167203 (2021).
- [74] J. Mildenerger, W. Mruzckiewicz, J. C. Halimeh, Z. Jiang, and P. Hauke, Probing confinement in a \mathbb{Z}_2 lattice gauge theory on a quantum computer, [arXiv:2203.08905](https://arxiv.org/abs/2203.08905).
- [75] M. Hanada, G. Ishiki, and H. Watanabe, Partial deconfinement, *J. High Energy Phys.* **03** (2019) 145.
- [76] M. Hanada and H. Watanabe, Partial deconfinement: A brief overview, *Eur. Phys. J.: Spec. Top.* **232**, 333 (2023).
- [77] V. Gautam, M. Hanada, J. Holden, and E. Rinaldi, Linear confinement in the partially-deconfined phase, *J. High Energy Phys.* **03** (2023) 195.
- [78] S. Kühn, J. I. Cirac, and M.-C. Bañuls, Quantum simulation of the Schwinger model: A study of feasibility, *Phys. Rev. A* **90**, 042305 (2014).
- [79] R. Jackiw and C. Rebbi, Vacuum periodicity in a Yang-Mills quantum theory, *Phys. Rev. Lett.* **37**, 172 (1976).
- [80] N. Batakis and G. Lazarides, Structure of the gauge theory vacuum at finite temperatures, *Phys. Rev. D* **18**, 4710 (1978).
- [81] G. 't Hooft, Computation of the quantum effects due to a four-dimensional pseudoparticle, *Phys. Rev. D* **14**, 3432 (1976).
- [82] Y.-P. Huang, D. Banerjee, and M. Heyl, Dynamical quantum phase transitions in U(1) quantum link models, *Phys. Rev. Lett.* **122**, 250401 (2019).
- [83] D. Marcos, P. Rabl, E. Rico, and P. Zoller, Superconducting circuits for quantum simulation of dynamical gauge fields, *Phys. Rev. Lett.* **111**, 110504 (2013).
- [84] T. Banks, L. Susskind, and J. Kogut, Strong-coupling calculations of lattice gauge theories: (1 + 1)-dimensional exercises, *Phys. Rev. D* **13**, 1043 (1976).
- [85] J. Kogut and L. Susskind, Hamiltonian formulation of Wilson's lattice gauge theories, *Phys. Rev. D* **11**, 395 (1975).
- [86] C. Gao, J. Liu, M. Chang, H. Pu, and L. Chen, Synthetic U(1) gauge invariance in a spin-1 Bose gas, *Phys. Rev. Res.* **4**, L042018 (2022).
- [87] C. Gao, Z. Tang, F. Zhu, Y. Zhang, H. Pu, and L. Chen, Non-thermal dynamics in a spin- $\frac{1}{2}$ lattice Schwinger model, *Phys. Rev. B* **107**, 104302 (2023).
- [88] J. Osborne, B. Yang, I. P. McCulloch, P. Hauke, and J. C. Halimeh, Spin-S U(1) quantum link models with dynamical matter on a quantum simulator, [arXiv:2305.06368](https://arxiv.org/abs/2305.06368).
- [89] W.-Y. Zhang, M.-G. He, H. Sun, Y.-G. Zheng, Y. Liu, A. Luo, H.-Y. Wang, Z.-H. Zhu, P.-Y. Qiu, Y.-C. Shen *et al.*, Scalable multipartite entanglement created by spin exchange in an optical lattice, *Phys. Rev. Lett.* **131**, 073401 (2023).
- [90] B. Yang, H.-N. Dai, H. Sun, A. Reingruber, Z.-S. Yuan, and J.-W. Pan, Spin-dependent optical superlattice, *Phys. Rev. A* **96**, 011602(R) (2017).
- [91] E. Gustafson and R. V. de Water, Improved Fermion Hamiltonians for quantum simulation, *PoS (LATTICE2023)*, 215 (2023).
- [92] X.-Q. Luo, Q.-Z. Chen, G.-C. Xu, and J.-Q. Jiang, Improved Hamiltonians for lattice gauge theory with fermions, *Phys. Rev. D* **50**, 501 (1994).